A Two Martian Years Survey of Water Ice Clouds on Mars with ACS onboard TGO

Aurélien Stcherbinine, Franck Montmessin, Mathieu Vincendon, Michael J. Wolff, Margaux Vals, Oleg Korablev, Anna Fedorova, Alexander Trokhimovskiy, Gaetan Lacombe, Lucio Baggio

A Two Martian Years Survey of Water Ice Clouds on Mars with ACS onboard TGO

Aurélien Stcherbinine[1,2], Franck Montmessin[2], Mathieu Vincendon[3], Michael J. Wolff[4], Margaux Vals[2], Oleg Korablev[5], Anna Fedorova[5], Alexander Trokhimovskiy[5], Gaetan Lacombe[2], Lucio Baggio[2]

[1]Department of Astronomy and Planetary Science, Northern Arizona University, Flagstaff, AZ 86011, USA
[2]LATMOS/IPSL, UVSQ Université Paris-Saclay, Sorbonne Université, CNRS, 78280 Guyancourt, France
[3]Institut d'Astrophysique Spatiale, Université Paris-Saclay, CNRS, 91405 Orsay, France
[4]Space Science Institute, 4750 Walnut Street, Suite 205, Boulder, CO, 80301, USA
[5]Space Research Institute (IKI), 84/32 Profsoyuznaya, 117997 Moscow, Russia

Key Points:

- Cloud altitude varies by 20 to 40 km between winter and summer, and between polar and midlatitudes.
- The GDS in MY 34 increases the altitude of the clouds by 10 to 20 km compared to the same season in MY 35.
- Clouds are predicted to be lifted at lower altitudes in the Mars PCM compared to ACS detections.

Corresponding author: Aurélien Stcherbinine, aurelien.stcherbinine@nau.edu

This article has been accepted for publication and undergone full peer review but has not been through the copyediting, typesetting, pagination and proofreading process, which may lead to differences between this version and the Version of Record. Please cite this article as doi: 10.1029/2022JE007502.

Abstract

The middle infrared (MIR) channel of the Atmospheric Chemistry Suite (ACS) instrument onboard the ExoMars Trace Gas Orbiter (TGO) ESA-Roscosmos mission has performed Solar occultation measurements of the Martian atmosphere in the 2.3–4.2 μm spectral range since March 2018, which now covers two Martian Years (MY). We use the methodology previously developed for the study of the MY 34 Global Dust Storm (GDS) (Stcherbinine et al., 2020) to monitor the properties (effective radii, extinction, altitude) of the Martian water ice clouds over the first two Martian years covered by ACS-MIR. The observations encompass the period $L_s = 163°$ in MY 34 to $L_s = 181°$ in MY 36. We determine that the typical altitude of the clouds varies by 20 to 40 km between the summer and winter, with a maximum extension up to 80 km during summer in the midlatitudes. Similarly, we also note that for a limited temporal range, the altitude of the clouds also varies by 20 to 40 km between the polar regions and the midlatitudes. We also compare observations acquired during the MY 34 GDS to observations from the same period in MY 35, using that latter as a reference to characterize the effects of this GDS on the clouds' properties. In addition, we compare our retrievals with the predictions of the Mars Planetary Climate Model (PCM), which shows a reasonable agreement overall for the altitude of the clouds, although the model usually predicts lower altitudes for the top of the clouds.

Plain Language Summary

We use data from the Middle InfraRed (MIR) channel of the Atmospheric Chemistry Suite (ACS) instrument onboard the ExoMars Trace Gas Orbiter mission, which has been probing the Martian atmosphere for two Martian years (MY), to study the properties of the water ice clouds in the Martian atmosphere. We observe that the clouds' altitude increases by 20 to 40 km during Summer and that they are also observed 20 to 40 km higher around the equator compared to the polar regions. This highlight the spatial and temporal diversity of the Martian water ice clouds, along with the large amplitude of the annual variations of the atmospheric structure. In addition, we contrast observations acquired during the Global Dust Storm (GDS) event of Summer 2018 (MY 34) with data from the following MY that we use as a reference to understand the effects of the GDS on the clouds, which reveals that the presence of the GDS increases the altitude of the clouds by 10 to 20 km. Finally, we compare our results to the predictions of the Mars Planetary Climate Model which shows a reasonable agreement overall, although the model tends to predict lower altitudes for the top of the clouds.

1 Introduction

Even though the role of water ice clouds in the Martian atmosphere was not well understood for many years after the Viking missions, they are now considered to play a major role in Martian climate and weather (Richardson, 2002; Montmessin et al., 2004; Navarro et al., 2014; Montmessin et al., 2017; Clancy et al., 2017; Vals et al., 2022; Rossi et al., 2022). Clouds perform an important role in the Martian water cycle as they are a major actor in the inter-hemispheric water exchange (Clancy et al., 1996; Montmessin et al., 2004, 2017). Similarly to atmospheric dust particles, water ice crystals also absorb and scatter incoming solar radiation, thus impacting the atmospheric structure and temperature (Wilson et al., 2007, 2008; Haberle et al., 2011; Madeleine et al., 2012; Navarro et al., 2014). In addition, the formation of clouds affects the ability of water (or hydrogen) to be further mobilized and to escape from the planet. However, more observational data are needed to better characterize the properties of water ice clouds in order to understand and model the evolution of the Martian atmosphere (Vals et al., 2018).

The formation of clouds in the atmosphere depends on several factors, such as the presence of water vapor, the pressure and temperature conditions, and the availability of condensation nuclei (Michelangeli et al., 1993; Montmessin et al., 2004). However, as water may exist in a supersaturated state in the Martian atmosphere (Maltagliati et al., 2011; Fedorova et al., 2020; Poncin et al., 2022), simply considering the freezing point for the condensation of atmospheric water is problematic. In addition, accurately predicting the distribution and the properties of airborne dust particles also remains a challenging aspect in current Global Climate Models (GCM) (Forget et al., 2014; C. Wang et al., 2018; D'Aversa et al., 2022). Thus, accumulating additional observations of the distribution and properties of the water ice crystals in the Martian atmosphere is required to further constrain the present-day clouds cycle, and its relationship to the Martian climate and water cycle.

The Atmospheric Chemistry Suite (ACS) instrument is a set of three spectrometers onboard the ExoMars Trace Gas Orbiter (TGO) ESA-Roscosmos spacecraft, which has been conducting science operations since March 2018 (Korablev et al., 2018, 2019; Vandaele et al., 2019). The Mid-InfraRed (MIR) channel is a high-resolution, cross-dispersion echelle spectrometer dedicated to solar occultation (hereafter "SO") geometry. Each observation covers a ∼300 nm wide spectral interval selected between 2.3 and 4.2 μm, which is set by rotating the secondary grating to one of the 10 positions (Trokhimovskiy et al., 2015; Korablev et al., 2018). The cross-dispersion optical scheme produces 10 to 21 stacked diffraction orders. The number and separation between the displayed orders depend on the secondary grating position. Considering the instantaneous angular field of view of the detector and its displacement during the integration time for each spectrum, ACS-MIR provides a sampling of the Martian atmosphere with a vertical resolution of ∼ 2.5 km.

Even though the primary objective of ACS and NOMAD is the study of the atmospheric trace gases in the Martian atmosphere, they also provide a unique dataset for the study of the distribution and properties of Martian aerosols (Stcherbinine et al., 2020; Luginin et al., 2020; Liuzzi et al., 2020, 2021; Streeter et al., 2022). In this paper we use ACS-MIR observations acquired in position 12 (i.e., ∼3.1–3.4 μm spectral range) to retrieve the properties of the Martian water ice clouds from the 3 μm water ice absorption band. Indeed, water ice atmospheric particles exhibit a specific signature due to the O-H stretching and bending that enables the distinction between water ice and bound water in dust. And as the depth and shape of the absorption feature depend on both the abundance and the sizes of the ice crystals, we can retrieve information on these quantities (Vincendon et al., 2011; Guzewich et al., 2014; Clancy et al., 2019). The methodology has already been developed and applied to observations conducted during the global dust storm (hereafter "GDS") of Martian Year (MY) 34. These efforts revealed very high altitude water ice hazes (up to 100 km) and large ice crystals (effective radius r_{eff} ∼1.5–2 μm) up to 65 km during the storm (Stcherbinine et al., 2020). ACS observations now cover two MY, one with and one without a GDS, for all latitudes, allowing us to observe the seasonal and spatial evolution of the Martian water ice clouds. In addition, observations acquired during MY 35 during the same L_s period when the GDS occurs in MY 34 also offer a reference to be compared to MY 34 GDS observations.

First, we briefly describe in Section 2 the ACS-MIR dataset and the methods used in this study. Sections 3 & 4 present the results of the annual monitoring of water ice clouds with their particle sizes and opacity, and Section 5 compares the retrieved vertical profiles of water ice clouds with results of GCM simulations from the Mars Planetary Climate Model (PCM) (Forget et al., 2022). Finally, Section 6 summarizes the main points of this study.

2 Data and methods

2.1 Dataset

Atmospheric transmittances are computed through ratios to measurements at 120 km above the surface, which is free from atmospheric absorption in this spectral range. Indeed, we observed in Stcherbinine et al. (2020) (where transmittances were computed relative to 150 km) that the haze top altitude only reaches 100 km during an extreme event like the MY 34 GDS, but without extending over 105 km. Data calibration and geometry calculations are described in Trokhimovskiy et al. (2020) and Olsen et al. (2021).

Since the publication of Stcherbinine et al. (2020), ACS-MIR has continued to acquire new data in the grating position 12, allowing us to observe the atmospheric 3 µm absorption band by covering the 3.1–3.4 µm spectral range (Korablev et al., 2018). We do not consider the observations acquired in the so-called "partial mode" (i.e., with a smaller number of diffraction orders) around the conjunction of Mars and Earth (when the downlink from the instruments is very limited). A total of 514 observations obtained between $L_s = 163°$ (MY 34) and $L_s = 181°$ (MY 36) were used in this study. The spatial and temporal distribution of these observations is shown in Figure 1. Due to the SO geometry, observations naturally occur in the periods near dawn and twilight.

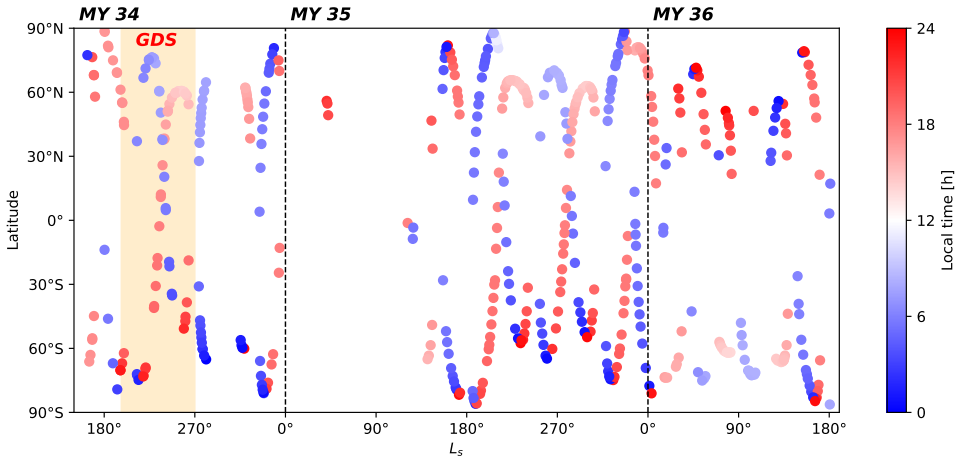

Figure 1. Spatial (latitude) and temporal (L_s and local time) distribution of the 514 ACS-MIR position 12 observations used in this study. The orange region corresponds to the period of the 2018/MY34 global dust storm.

2.2 Continuum spectra

Based on the methodology previously described in Stcherbinine et al. (2020), we extract the spectral continuum for each observed altitude from the 20 spectral segments (i.e., diffraction orders) that compose the ACS-MIR observation (Korablev et al., 2018; Trokhimovskiy et al., 2015). For each diffraction order, we use successive iterations of a median filter and a second-degree polynomial fit on the 200 centered points to determine the transmission level of the spectral continuum at the center of the diffraction order, while minimizing the effects of contamination by the gas absorption bands or the broad instrumental curvature that affects the orders. This results (for each observed altitude) in a spectrum with one point per diffraction order, with a

spectral resolution of $\Delta\lambda \sim 20$ nm. To avoid detector edges effects, we only consider the center of each diffraction order to process the extraction. We also ignore the outer regions of the extracted spectra, that is, the spectels corresponding to 3.10, 3.12, and 3.44 µm.

We have updated the uncertainties estimation for the ACS-MIR transmittances. Thus, as we are considering the center of each diffraction order, we include an uncertainty of ±5% of the transmission value to account for the uncorrected straylight that affects the data in position 12 (Trokhimovskiy et al., 2020).

We compute the haze top altitude (i.e., the highest altitude at which aerosols can be detected along the line of sight), defined here as the first altitude for which the transmission is greater than 0.98 over the entire spectrum, along with the extinction coefficient k_{ext} for each wavelength (forming an extinction spectrum) and altitude from the total optical depth (i.e., integrated along the line of sight, $\tau = -\log(\text{Tr})$) using a vertical profile inversion algorithm based on the onion-peeling method (Goldman & Saunders, 1979) as described in sections 2.2 and 2.4 of Stcherbinine et al. (2020).

2.3 Water ice particle size retrieval method

To identify the Martian water ice clouds in our observations, and constrain their particle sizes, we compare each retrieved extinction spectrum with models of the extinction coefficient's wavelength dependence for either water ice or dust spherical particles (Stcherbinine et al., 2020). These theoretical extinction coefficients are computed using a public domain Mie code (Toon & Ackerman, 1981) and assuming a gamma size distribution (Hansen & Travis, 1974) with an effective variance of 0.1 (e.g., Wolff et al., 2017, and references contained within).

To avoid the problem of the presence of local minima for r_{eff} during the fitting process, we generate models on a grid of radii of 0.01 between 0.1 and 8 µm, and for each one we compute the χ^2 and Δ^2 values defined in equations (2) & (3), which quantify the deviation between the data and the model. Finally, we have slightly adjusted the criterion for the detection and characterization of the atmospheric water ice particles compared to Stcherbinine et al. (2020). This modification results from a better understanding of detection biases thanks to the new larger dataset, and also accounts for the new uncertainty estimate (section 2.2). The new criterion is as follows:

$$\left(\chi^2_{\nu,\,\text{ice}} < 1\right) \,\&\, \left(\frac{\Delta^2_{\text{dust}}}{\Delta^2_{\text{ice}}} > 4\right) \tag{1}$$

Where

$$\chi^2_\nu(r_{\text{eff}}) = \frac{1}{N-2}\sum_{i=1}^{N}\frac{\left(\text{data}_i - \text{model}_{r_{\text{eff}},\,i}\right)^2}{\sigma_i^2} \tag{2}$$

and

$$\Delta^2(r_{\text{eff}}) = \frac{1}{N-2}\sum_{i=1}^{N}\left(\text{data}_i - \text{model}_{r_{\text{eff}},\,i}\right)^2 \tag{3}$$

Notation

$\mathbf{data_i}$ The i^{th} spectel of the k_{ext} spectra from the ACS-MIR observation.
$\mathbf{model_{r_{eff},\,i}}$ The i^{th} spectel of the model extinction spectra for a particle size of r_{eff}.
$\boldsymbol{\sigma_i}$ The uncertainty on the value of data_i.
$\boldsymbol{N}$ The number of spectral points in the considered spectrum.

Specifically, we require that:

1. the modeled extinction spectrum using water ice provides a good fit to the observational data, including the spectrum uncertainties $\left(\chi^2_{\nu,\,\mathrm{ice}} < 1\right)$.
2. the water ice model provides a significantly better solution than the best fit that can be obtained with a dust model. So we consider only water ice models with a mean square difference to the data lower than the one of the best dust model by at least a factor 4. This factor 4 has been determined experimentally by visual comparison between the models and the data for many spectra, to retain only those which match within the errorbars.

For each spectrum where water ice crystals are detected, we retrieve the optimal r_{eff} as the one corresponding to the model associated with the lower $\chi^2_{\nu,\,\mathrm{ice}}$ that verifies equation (1). Then, the lower (respectively upper) bound for the particle size uncertainties corresponds to the minimum (respectively maximum) value of r_{eff} in the set of models associated with $\chi^2_{\nu,\,\mathrm{ice}}$ and Δ^2_{ice} that prove equation (1).

3 Cloud monitoring

In sections 3.1 and 3.2, we present the results of the analysis of the new data, as described in Stcherbinine et al. (2020). They cover a complete year without a GDS, from $L_s = 140°$ (MY 35) to $L_s = 182°$ (MY 36). This range corresponds to ACS-MIR operating in full-observation mode (cf. Figure 1). Then, we compare this new dataset to the previous one for the GDS year MY 34 in section 3.3.

In the following, a "profile" refers to one set of ACS-MIR observations from the surface to the haze top, while a "cloud" corresponds to contiguous water ice detections within a profile. Additionally, as we observe the presence of water ice clouds up to the haze top altitude in most of the profiles, we consider the haze top equivalent to the maximum altitude of the water ice clouds. Also, our water ice clouds detections extend typically over ~ 20 km below their maximum altitude, thus we will only discuss in this section the maximum altitude of the water ice clouds as it is representative of the overall behavior of the water ice clouds (and the maximum altitude of the aerosols in general).

3.1 Seasonal variations

We show seasonal variations for three distinct latitude ranges in Figure 2 in order to delineate the seasonal variations from the latitudinal dependency of the clouds that will be discussed in paragraph 3.2.

As reported in previous studies (e.g., Clancy et al., 2019; Stcherbinine et al., 2020; Luginin et al., 2020; Liuzzi et al., 2020), we find a decrease in the size of the water ice crystals as altitude increases, both from an individual cloud and from a global perspective (cf. Figures 2, 3 & 4). In addition, clouds are usually found at the top of the profiles, capping the layers composed of other types of aerosols (dust or large ice crystals below).

We also observe in Figure 2 that if the maximum altitude of the clouds fluctuates with season (Jaquin et al., 1986; Forget et al., 1999; Montmessin et al., 2006; Heavens et al., 2011; Määttänen et al., 2013; Smith et al., 2013), the observed variations depend on the latitude. Indeed, at equatorial latitudes ($45°\mathrm{S} \leq \mathrm{lat} \leq 45°\mathrm{N}$, panel b), we observe the presence of water ice crystals up to 83 km around the perihelion ($L_s \sim 270°$), while the maximum altitude of the clouds does not exceed 50 km at $L_s \sim 80°$. Plus, for latitudes southward 45°S (panel c) we note an increase of the maximum altitude of the clouds that goes from 30 km at $L_s \sim 160°$ to 80 km at $L_s \sim 260°$, followed by a

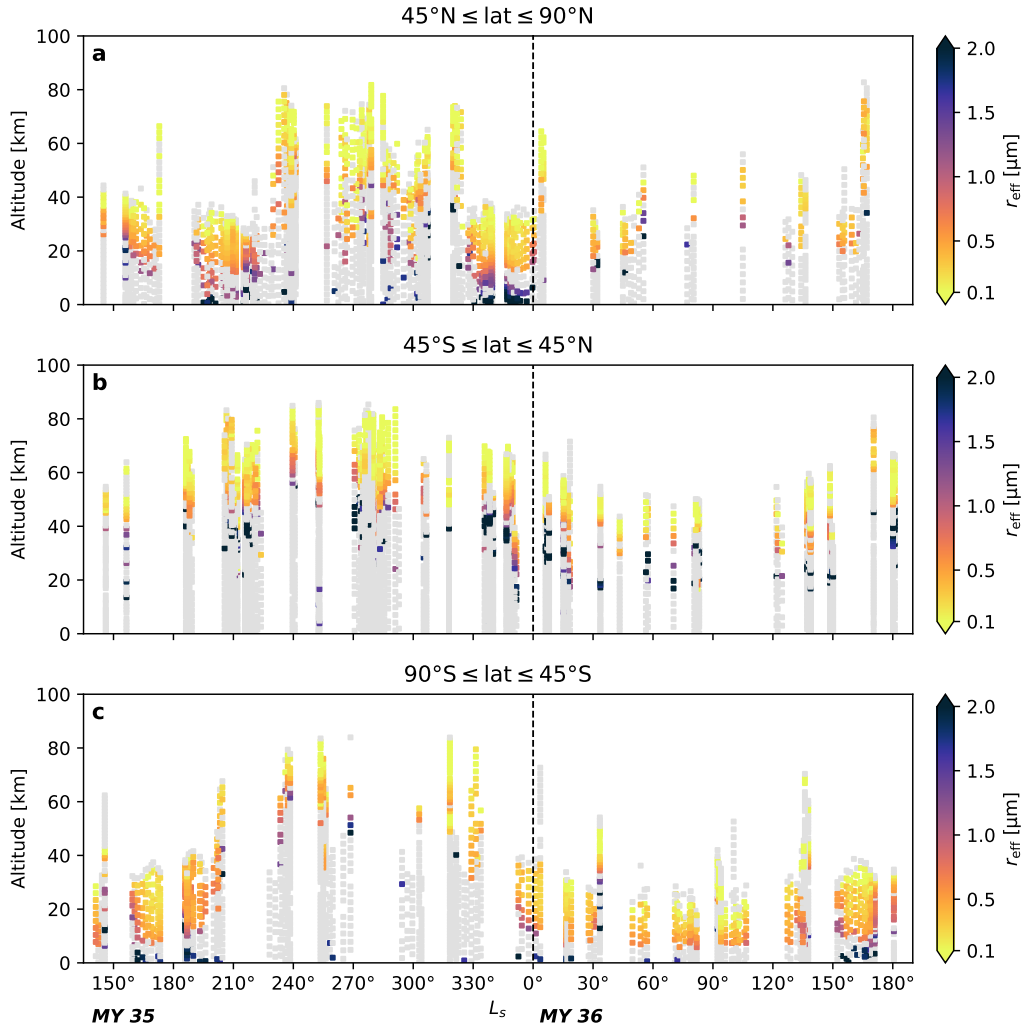

Figure 2. Vertical profiles of water ice clouds in the Martian atmosphere as observed by ACS-MIR over mid-MY 35 to mid-MY 36, with their crystal size determined using the method presented in section 2.3. Each panel represents the profiles grouped by ranges of latitude (North/Equatorial/South). Observations without water ice detections are in gray.

decrease from $L_s \sim 330°$ that brings it back to 30 km at $L_s \sim 20°$. Symmetrically, in the Northern hemisphere, between 45°N and 90°N (panel a) the maximum altitude of the clouds moves from 35 to 20 km between $L_s = 145°$ and $L_s = 215°$, and from 20 to 40 km between $L_s = 30°$ and $L_s = 100°$ before coming back to 25 km at $L_s = 160°$.

Observation of a regional dust storm

In addition to these variations of the water ice clouds altitude with L_s, we observe in the Northern hemisphere (for latitudes greater than 45°N; Figure 2a) a sudden increase of their maximum altitude between $L_s = 236°$ and $L_s = 323°$, which indicates the presence of a regional dust storm in this region. This dust storm and its impact on the altitude of the water ice clouds have also been observed by the NOMAD instrument and are reported in Streeter et al. (2022). Indeed, from $L_s = 225°$ to $L_s = 240°$ the maximum altitude of the clouds goes from 35 to 80 km. That is to say, there is an increase in the altitude of the water ice clouds of about 40 km while the latitude of the observations remains similar (between 60°N and 65°N, cf Figure 1). The clouds remain in these high atmospheric layers (with crystals observed up to 80 km) until $L_s = 325°$, even though we can observe a progressive decrease of the maximum altitude of the clouds over the storm, which goes from 80 to 65 km between $L_s = 235°$ and $L_s = 305°$ while the observed latitudes oscillate between 41°N and 63°N. Then, the maximum altitude of the water ice clouds suddenly decrease between $L_s = 323°$ and $L_s = 328°$, going from 71 to 28 km. However, as 10° of latitude separate these two observations (61.5°N for $L_s = 323°$ and 71.5°N for $L_s = 328°$, plus, 71.5°N is above the northernmost latitude of the observations of the storm), it is challenging to determine precisely the end date of the dust storm with our observations. For example, the northern limit of the MY 34 GDS was very abrupt and located under similar latitudes (Stcherbinine et al., 2020). In addition, 71.5°N is also close to the typical boundary of the north polar vortex at this period (Ball et al., 2021), which may act as an efficient barrier to the latitudinal transport of atmospheric particles (Toigo et al., 2020).

Regarding the temporal behavior of this dust storm, we observe that it occurs in the second half of the "dust storm season", which illustrates the diversity of Martian dust storms and the necessity to observe and study a large number of these events (H. Wang & Richardson, 2015; Battalio & Wang, 2021). We also observe that this storm does not push clouds to altitudes as high as what has been observed during the MY 34 GDS (80 km here vs 100 km during the GDS), and that no water ice crystals larger than 1.5 µm are observed above 40 km, unlike during the GDS where such large crystals have been detected between 50 and 65 km.

3.2 Latitudinal variations

As mentioned above, and reported in previous studies (Jaquin et al., 1986; Forget et al., 1999; Montmessin et al., 2006; Heavens et al., 2011; Smith et al., 2013) the vertical structure of Martian aerosols depends on the latitude. To isolate this latitudinal dependence from the seasonal variation discussed in section 3.1, Figure 3 presents the vertical profiles of water ice crystals size within the clouds. We adjust several L_s bins to minimize the impact of the seasonal variations while providing enough coverage in terms of latitude. If the entire range of latitudes is not covered in each panel, we can observe on panels a, c & d that the altitude of the water ice clouds (and more generally of the Martian aerosols) increases when getting closer to the equator. This also produces a bell-shaped distribution of the altitude of the clouds as a function of latitude. Indeed, we observe on Figures 3 & 4 that if the water ice crystals with radius $r_{\text{eff}} \leq 1$ µm are located between 10 and 40 km in the polar regions ($> 60°$N or $< 60°$S), they are found typically between 30 and 80 km around the equator, and occasionally up to 85 km.

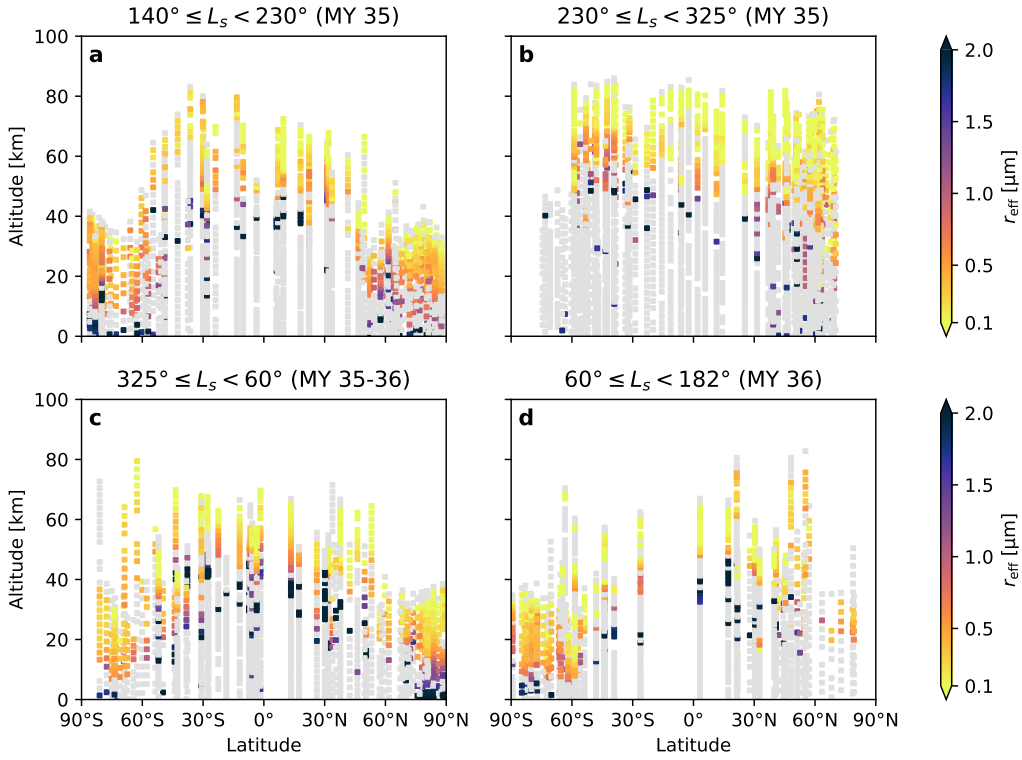

Figure 3. Vertical profiles of water ice clouds in the Martian atmosphere as observed by ACS-MIR between $L_s = 140°$ (MY 35) and $L_s = 182°$ (MY 36) as a function of the latitude of the observation. To highlight the latitudinal variations of the clouds while removing their seasonal dependence (discussed in section 3.2), each panel represents the profiles grouped by L_s ranges. Observations without water ice detection are in gray.

Another noteworthy point regarding the size of the water ice crystals that compose the clouds detected by ACS-MIR: we observe that for a fixed size of particle, the altitude of the detections still follows the bell-shaped distribution with latitude already identified for the general distribution of the clouds in the previous paragraph. Thus, there is no strict correlation between the size of a crystal and its altitude in the atmosphere. Other parameters have to be considered, such as the latitude of the cloud. This is consistent with the decrease of the scale height of the atmosphere in the high latitudes, where the temperatures are lower. As the temperatures decrease with increasing latitude, one finds a decrease in the cloud altitudes. However, we observe in Figure 4 that we also do not detect crystals with radius ≥ 1.5 µm above 55 km (outside the MY 34 GDS), there is no crystal with size ≤ 0.2 µm at altitudes lower than 15 km. Plus, except for one atypical cloud observed by 35°S of latitude and 252° of L_s (MY 35), only crystals with sizes ≤ 0.1 µm populate the altitudes higher than 80 km. Thus, we can identify with Figure 4 the range of altitudes that are populated by water ice crystals for a given radius.

Regarding the larger crystals ($r_{\text{eff}} \geq 1.5$ µm), they dominate the lower layers of the clouds and are observed up to 55 km of altitude around 30°S. However, such particles are not observed for all profiles in which a water ice cloud has been detected, unlike small-grained high altitude hazes that are observed at the top of almost every profile. The localized aspect together with the observed altitudes of these clouds

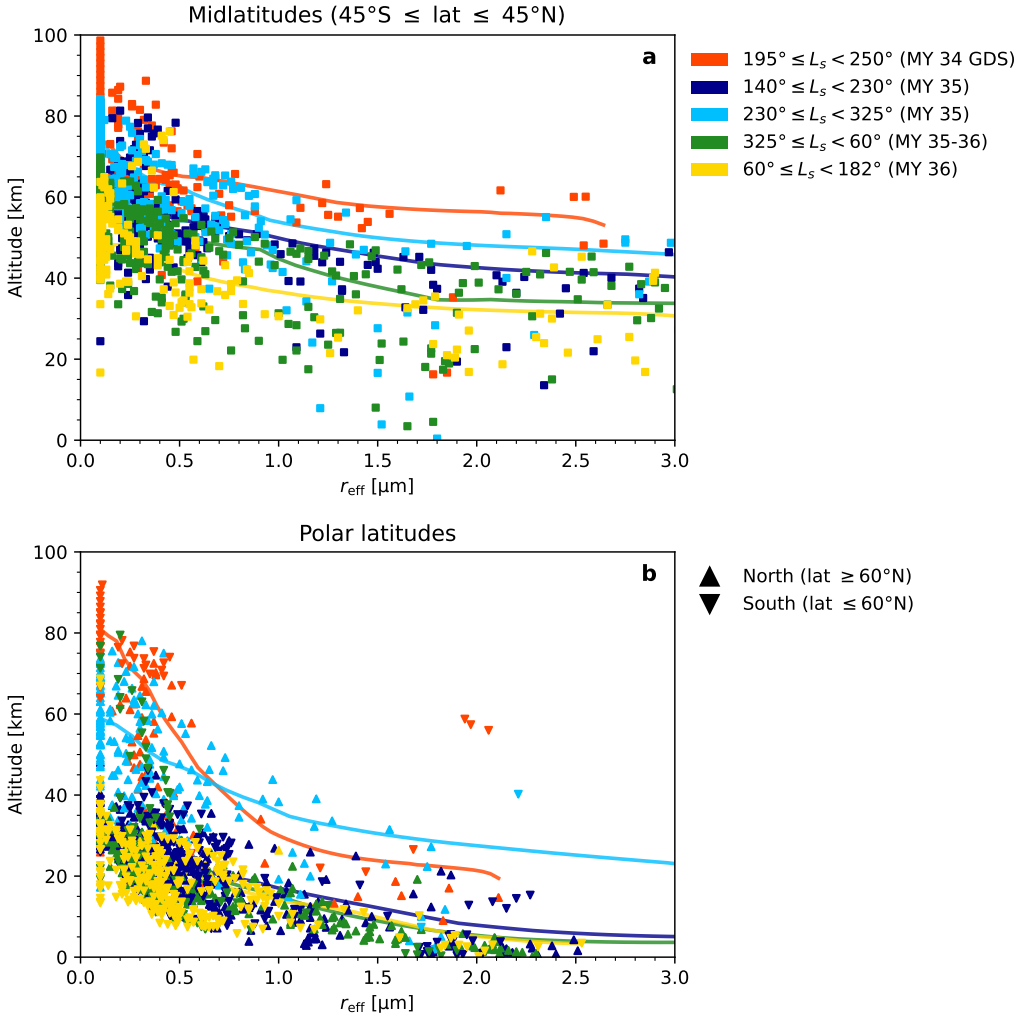

Figure 4. Distribution and size of the water ice crystals within the clouds as a function of their altitude and L_s of observation, for 3 ranges of latitude: midlatidudes (panel a), Northern and Southern polar latitudes (panel b). The solid lines show the average trend for each range of L_s Observations acquired during the MY 34 GDS are shown in red for comparison with data from non-GDS years (MY 35 & 36).

composed of crystals with $r_{\text{eff}} \sim 2$ µm is consistent with the results obtained using CRISM limb observations presented in figures 10 to 17 of Smith et al. (2013).

Concerning the local dust storm occurring in the Northern hemisphere during MY 35 (cf. section 3.1), panel b of Figure 3 presents profiles of clouds acquired during this period. This event allows us to study its specific impact on the clouds in the Northern latitudes in relation to the rest of the planet. Although TGO's orbit over this period did not allow ACS to probe latitudes above 65°S and 70°N, we observe that the maximum altitude of the clouds observed near 70°N extends to 70 km, which is higher than clouds observed at these latitudes outside of the storm (cf. panels a, c & d of Figure 3), but lower than the altitudes of the mesospheric clouds between 40°S and 20°N (Clancy et al., 2019).

3.3 Comparison with the 2018/MY34 GDS

Stcherbinine et al. (2020) used the early observations provided by ACS-MIR to study the planetary-scale dust storm that encircled Mars during MY 34. With the current extended dataset, it is now possible to compare observations acquired during the MY 34 GDS with the ones obtained for the same range of L_s in MY 35, when there was no GDS.

Figure 5 presents a superimposition of the profiles obtained between $L_s = 190°$ and $L_s = 250°$ during MY 34 (panels a & e) and MY 35 (panels b & f). The latitudes and local times of the observations are indicated in panels c, d, g & h respectively. This information should be taken into account when comparing the two years, as the latitude of the clouds has a significant impact on its profile characteristics (cf. section 3.2). Even when the two datasets cover the same latitude range, we note in Figures 4 & 5 that the altitude of the clouds for MY 35 does not exceed 85 km (consistent with the results presented in Clancy et al. (2019)), while small-particle clouds ($r_{\text{eff}} \leq 0.1$ µm) are observed up to 100 km at the beginning of the GDS. In particular, we observe at the onset of the GDS ($L_s = 195.5°$, MY 34) a profile in the Southern hemisphere (62°S) with a cloud that extends up to 92 km along with large water ice crystals ($r_{\text{eff}} \sim 2$ µm) around 58 km, which contrasts with the observations acquired under the same conditions during MY 35 with clouds that do not extend over 40 to 50 km.

The period around $L_s \sim 240°$ in the Northern hemisphere is also interesting, It not only corresponds to the end of the MY 34 GDS, but also to the maximum of dust activity for a regular (i.e., without GDS) year (Lemmon et al., 2015). We also note the presence of a regional dust storm during this period in MY 35 (cf. section 3.1). We observe that the maximum altitudes of the clouds are quite similar in both cases, i.e., between 70 and 85 km. However, we do not observe the large water ice crystals ($r_{\text{eff}} > 1$ µm) during the MY 35 dust storm that were seen between 50 and 60 km in MY 34 during the GDS.

Regarding the larger water ice crystals ($r_{\text{eff}} \sim 1.5 - 2$ µm), whose detection between 55 and 65 km during the GDS was surprising (Stcherbinine et al., 2020), similar sizes can be observed up to 55 km in the equatorial regions in MY 35 (i.e., no GDS). However, these larger crystals generally remain confined to altitudes below 50 km. For smaller particle sizes ($r_{\text{eff}} \sim 1 - 1.5$ µm), we observe that while the detections during the GDS are mostly concentrated around 60 km of altitude, they are typically found near 50 km during the same period in MY 35 (cf. Figure 4). Similarly, we also observe in Figure 5 that the detections of water ice crystals with sizes 0.13 µm $\leq r_{\text{eff}} \leq 0.5$ µm that are detected between 75 and 85 km during the GDS (panel a) are not present in the following year (panel b), where this size of crystals is not observed above 75 km. Thus, the increase of the average altitude of the clouds during the GDS does not affect all the ice particles in the same way, rather it depends on their size:

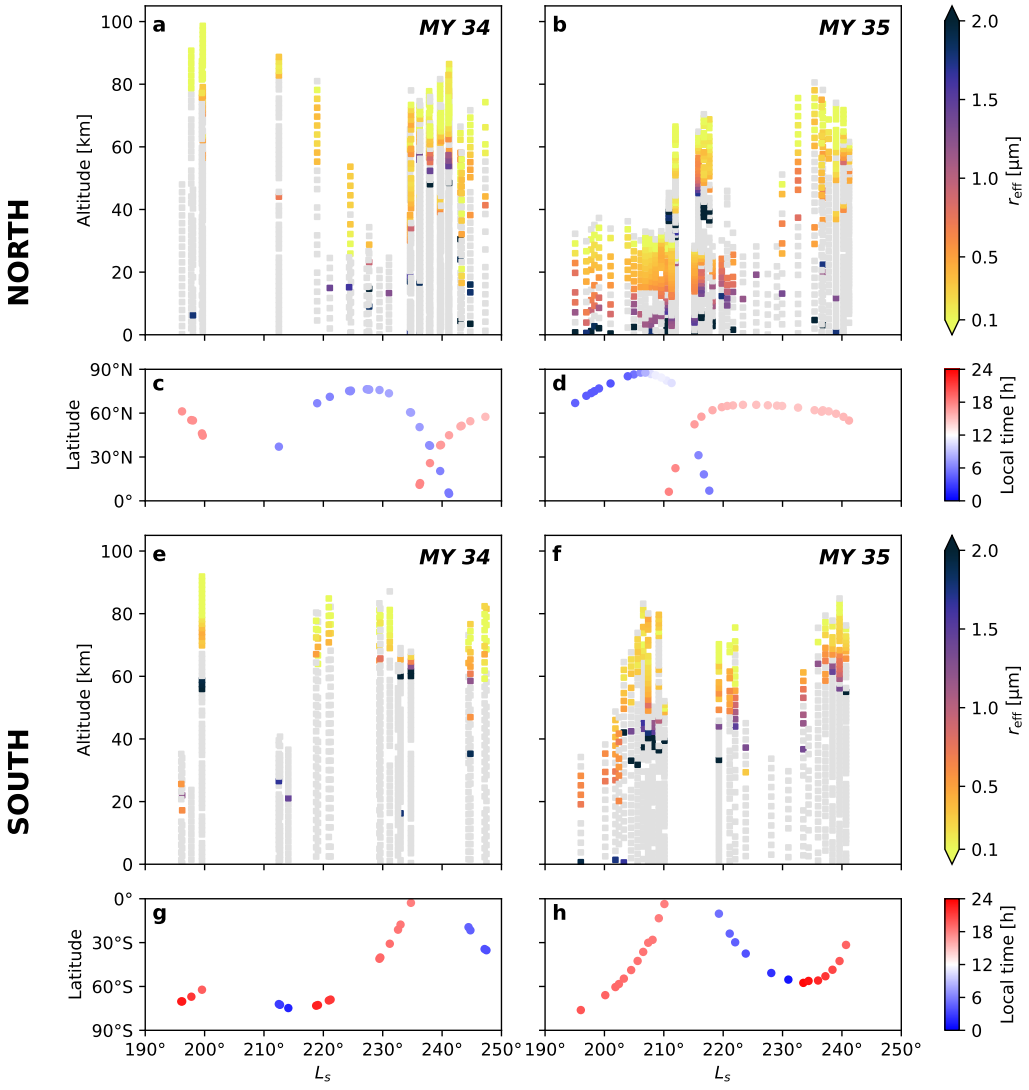

Figure 5. Vertical profiles of water ice clouds in the Martian atmosphere as observed by ACS-MIR between $L_s = 190°$ and $L_s = 250°$ over MY 34 (a & e) and MY 35 (b & f). Panels (c, d, g & h) indicate the latitudes and local times of the observations presented in panels (a, b, e & f) respectively. Observations without water ice detection are in gray.

the increase of the maximum altitude of the smallest crystals ($r_{\text{eff}} \leq 0.1$ µm) is 20 km more during the storm, and only 10 km for those between 0.1 and 0.5 µm.

We also observe that the impact of the MY 34 GDS on the clouds and aerosols is stronger at high latitudes than in the equatorial region. Indeed, it has been reported that the altitude of clouds does not vary as a function of latitude during the GDS, which tends to homogenize the vertical structure of the atmosphere across the planet (Stcherbinine et al., 2020; Luginin et al., 2020; Liuzzi et al., 2020). This effect is particularly visible in the Southern hemisphere (panels e to h of Figure 5). Thus, while the typical maximum altitude of equatorial clouds varies from $\sim$ 80 km to $\sim$ 90 km during the GDS, it moves from $\sim$ 40 to $\sim$ 80 km for latitudes poleward of 60°S and 60°N. In addition, Figure 4b shows that the detections of 2 µm ice crystals at 60 km during the GDS in the Southern latitudes are significantly higher than all the other detections in MY 35 that usually do not exceed 20 km of altitude for this particle size. Although one exception is a cloud with crystals of $r_{\text{eff}} = 2.2$ µm detected at 40 km in the Southern hemisphere at $L_s = 321°$ (MY 35), which is still 20 km below the altitude where such clouds were detected during the GDS.

4 Aerosols extinction

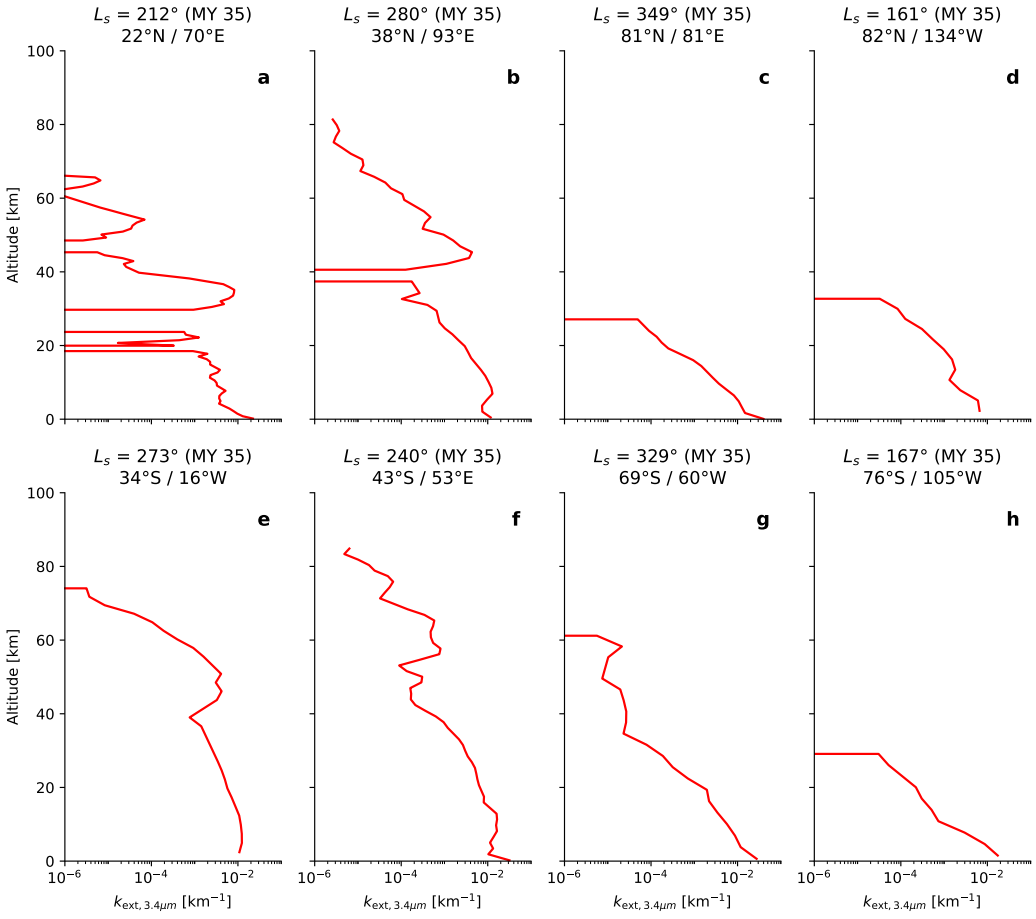

Figure 6. Vertical profiles of the derived extinction coefficient k_{ext} at $\lambda = 3.4$ µm from 8 different ACS-MIR observations acquired during MY 35 at various latitudes. The light blue areas represent the altitudes where water ice clouds have been identified.

4.1 Study of individual profiles

Along with particle size, the extinction coefficient is an important property. It will influence the amount of incoming solar energy that will be thermally transferred to the atmosphere (Gierasch & Goody, 1972; Montmessin et al., 2002; Madeleine et al., 2011, 2012). The SO geometry used by ACS-MIR gives us direct access to the vertical profiles of the atmospheric extinction at each observed wavelength through the vertical inversion technique. In fact, as described in Section 2 and Stcherbinine et al. (2020), this step has already been performed as part of our derivation of the properties of the water ice clouds.

Figure 6 shows 8 extinction profiles at $\lambda = 3.4$ µm acquired by ACS-MIR at various latitudes during MY 35, showing altitudes where water ice particles have been detected in each profile. Because 3.4 µm is located on the edge of the 3 µm band, it is less sensitive to the composition of the atmospheric layer (water ice or dust) and to the size of the water ice crystals (Vincendon et al., 2011). As a result, it is more indicative of the general aerosol extinction of the atmosphere (compared to the extinction at 3.2 µm that highlight the presence of small-grained water ice crystals). We observe a difference between polar latitudes (c, d, g & h) and more tropical or equatorial observations (a, b, e & f). Indeed, while the main cloud layers are typically observed above 50 km in the equatorial profiles, we also note the presence of additional layers at lower altitudes (around 10 km). This is particularly clear in profile b, where the extinction goes from $7 \cdot 10^{-3}$ km^{-1} at 3 km to $1.3 \cdot 10^{-2}$ km^{-1} at 7 km before progressively decreasing to 10^{-4} km^{-1} at 40 km. Then, the extinction increases again up to $4 \cdot 10^{-3}$ km^{-1} between 40 km and 52 km, which corresponds to the bottom of the water ice layer that extends from 47 km to 82 km. The presence of multiple high-extinction layers has been previously observed by SPICAM (Spectroscopy for the Investigation of the Characteristics of the Atmosphere of Mars) onboard Mars Express (Fedorova et al., 2009, 2014).

We also note in profiles b & e that we only detect water ice crystals in the upper part of the detached layers and above, which means that the lower altitudes of these layers are primarily composed of either dust or large water ice crystals. Similarly, we observe in profile a some detections of large ($r_{\text{eff}} = 1.5 - 3$ µm) water ice crystals between 23 km and 36 km of altitude, which suggests the presence of water ice and not only dust in these lower layers. This vertical structure of ice layers capping the dust layers has already been reported with limb observations (Smith et al., 2013). In addition, clouds are detected at the top of the profiles associated with extinction down to a few 10^{-5} km^{-1}. The detection of these very tenuous water ice hazes is made possible by the high sensitivity provided by ACS-MIR and the SO geometry technique.

4.2 Latitudinal variations

Figures 7 & 8 present vertical profiles of the extinction coefficient k_{ext} at 3.4 µm acquired by ACS-MIR between $L_s = 140°$ (MY 35) and $L_s = 90°$ (MY 36), filtered by latitude and L_s to highlight the seasonal and latitudinal variations of the atmospheric vertical structure (similarly to Figures 2 & 3). We observe in Figure 7, similarly to what has been noted above for the global behavior of the clouds, that there is a strong latitudinal dependence in the atmospheric extinction profiles: a given k_{ext} value is observed at higher altitude close to the equator than in the polar regions. This is in agreement with previous retrievals of the atmospheric dust extinction from Mars Climate Sounder observations (Kleinböhl et al., 2015). This variation is only about 10 km for the lower layers of the atmosphere, but between $\sim$ 30°S and 55°N we observe in most of our profiles the presence of a second detached atmospheric layer (i.e., atmospheric extinction decreases with altitude then increases again by at least one order of magnitude) around ∼30–55 km (as previously noted in individual profiles

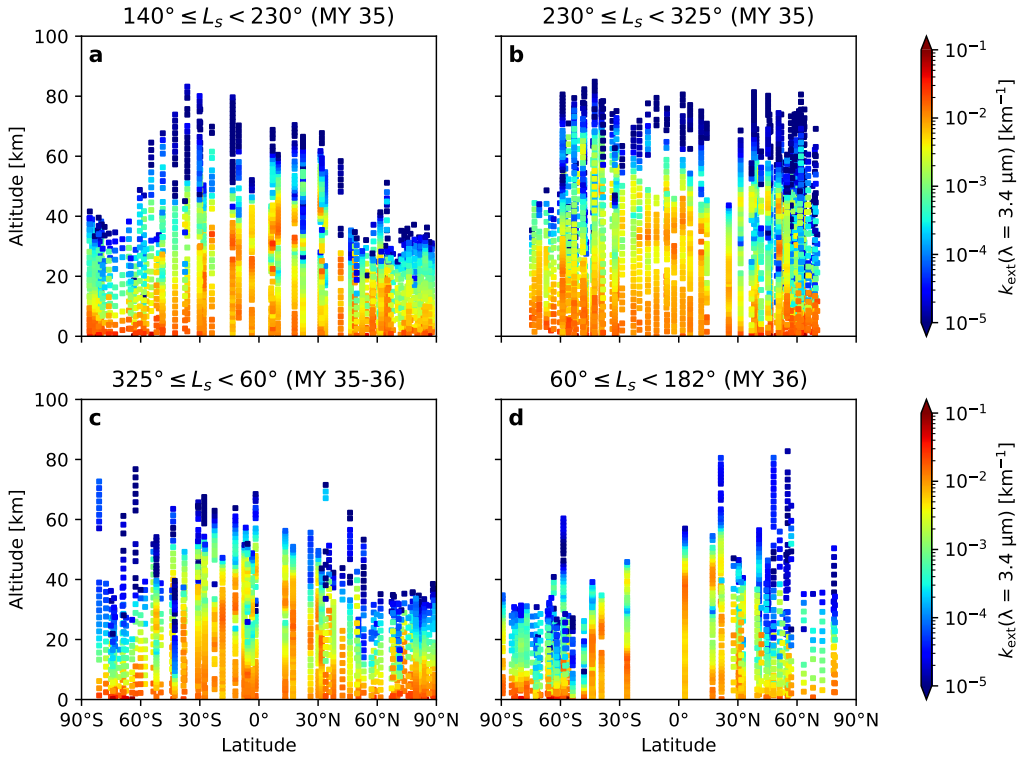

Figure 7. Vertical profiles of the measured extinction of the Martian atmosphere ($k_{\text{ext}} = d\tau/dz$, in km^{-1}) at 3.4 μm as observed by ACS-MIR between $L_s = 140°$ (MY 35) and $L_s = 182°$ (MY 36) as a function of the latitude of the observation. To highlight the latitudinal variations of the clouds by getting rid of their seasonal dependency (discussed in section 3.2), each panel represents the profiles grouped by ranges of L_s.

from Figure 6). Thus, extinction values of $\sim 10^{-2}$ km^{-1} can be observed up to 50 km (i.e., 40 km above the altitude where they are observed around 60°N/S) in these layers. This suggests that when a large quantity of aerosols are raised above a certain altitude in the atmosphere ($\sim$ 30 km) they do not remain in one single atmospheric layer but are split in two distinct layers, with a significant decrease of the atmospheric extinction (by one order of magnitude) between them.

4.3 Seasonal variations

Along with the latitudinal variations, we also present in Figure 8 the evolution of the atmospheric extinction profiles with the L_s. We observe that the variations of altitude for a given extinction value are of lower amplitude than the variations of the average water ice clouds altitude for the same profiles (cf. section 3.1). Between 90°S and 55°S (panel c), the altitude where $k_{\text{ext}} \sim 5 \cdot 10^{-3}$ km^{-1} goes from 5 km at $L_s = 180°$ to 30 km at $L_s = 320°$, and then back to 5 km at $L_s = 30°$. We also note that when the haze top altitude increases, for a fixed range of latitudes, it is largely due to the expansion of low-extinction layers to the higher altitudes rather than a shift of the vertical structure of the extinction profile, i.e., a given extinction value remains approximately associated with the same altitude, but layers with lower k_{ext} values appear at the top of the profiles, which is coherent with NOMAD/IUVS

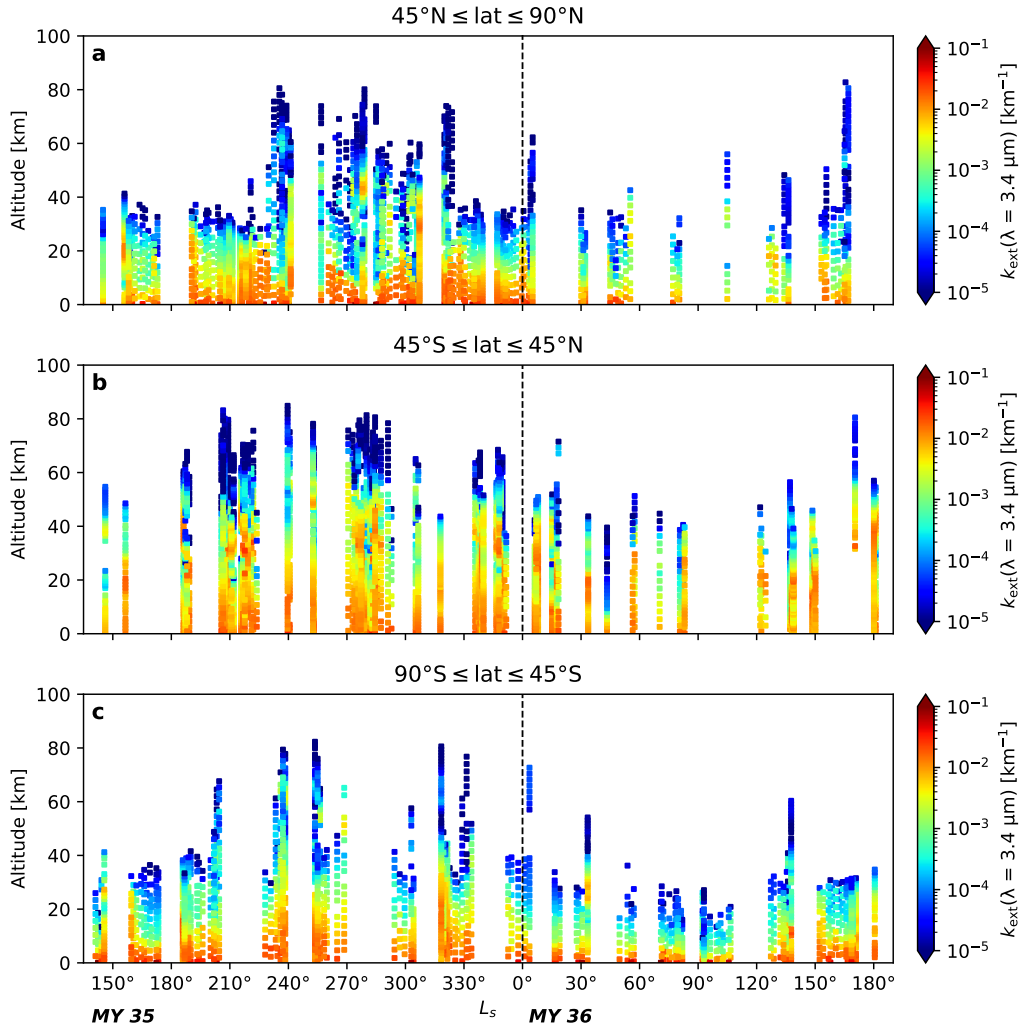

Figure 8. Vertical profiles of the measured extinction of the Martian atmosphere ($k_{\text{ext}} = d\tau/dz$, in km^{-1}) at 3.4 µm as observed by ACS-MIR over mid-MY 35 to mid-MY 36. To highlight the seasonal variations of the clouds by getting rid of their latitudinal dependency, each panel represents the profiles grouped by ranges of latitude (North/Equatorial/South).

measurements over MY 35 (Streeter et al., 2022) and previous SPICAM observations from MY 27 to MY 31 (Määttänen et al., 2013).

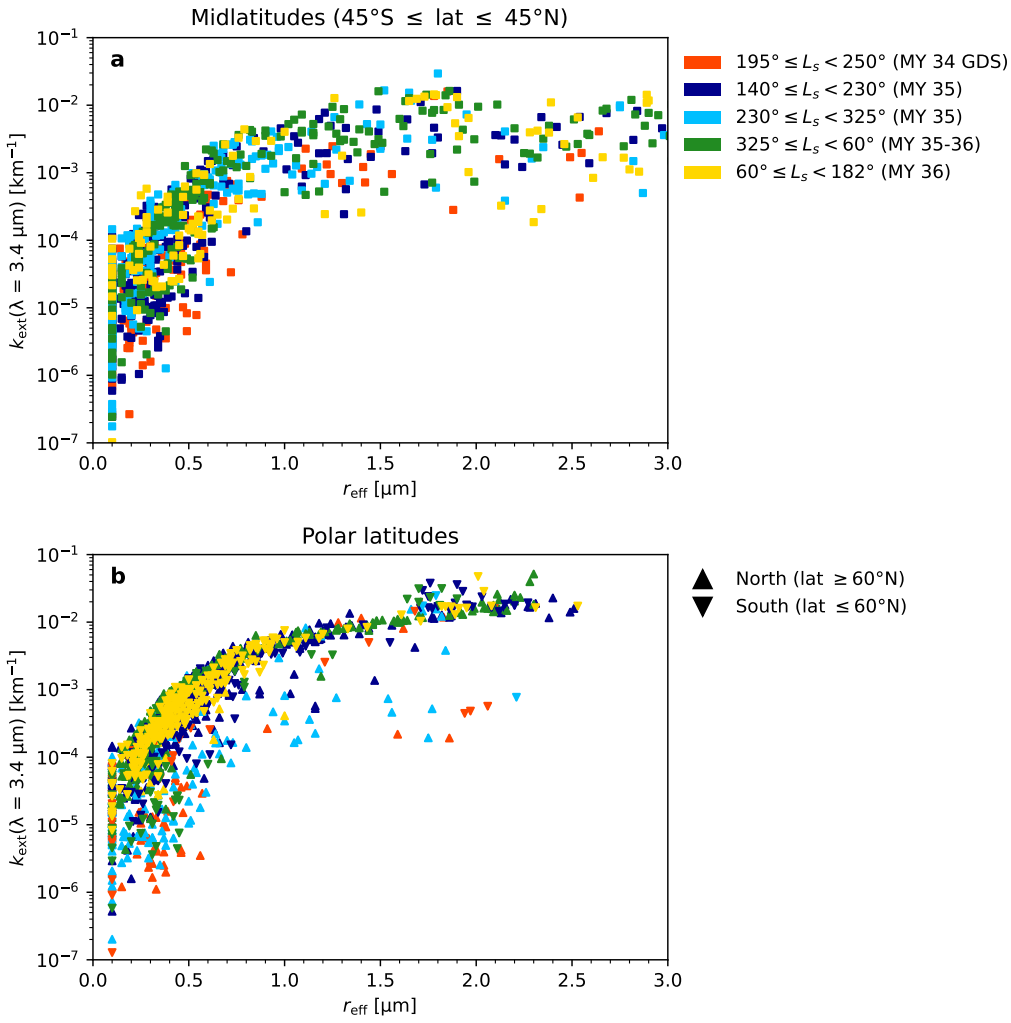

Figure 9. Distribution and size of the water ice crystals within the clouds as a function of their extinction coefficient k_{ext} and L_s of observation, for 3 ranges of latitude: midlatidudes (panel a), Northern and Southern polar latitudes (panel b). Observations acquired during the MY 34 GDS are shown in red for comparison with data from non-GDS years (MY 35 & 36).

4.4 Extinction vs crystal size

Figure 9 presents the extinction coefficient k_{ext} of the clouds at $\lambda = 3.4$ µm as a function of the retrieved size of the water ice crystals r_{eff} for 3 ranges of latitudes (midlatitudes, northern and southern polar latitudes) and 5 ranges of L_s, including the MY 34 GDS. We observe at all latitudes the presence of 2 regimes depending on the size of the water ice crystals: for $r_{eff} \leq 1$ µm the extinction k_{ext} increases with r_{eff}, while for larger particles the extinction of the clouds remains in the same range of values when r_{eff} varies between 1.5 and 3 µm.

We can still note that, if we exclude the data from the MY 34 GDS and the MY 35 dust storm (discussed further in the next paragraph), the points in the polar regions (panel b) have less scatter in terms of k_{ext} than in the midlatitudes (panel a), especially for the large particles ($r_{\text{eff}} \geq 1.5$ μm). This may be related to the smaller variations of the cloud altitudes in these regions (cf. Figure 4), which suggests a more stable vertical distribution of the properties of the clouds (both k_{ext} and r_{eff}). Also, for fixed values of r_{eff} and λ the extinction coefficient k_{ext} is solely a function of the number of particles that have scattered the light along the line of sight. Thus, the small dispersion in the cloud extinction values in the polar regions indicates that the number density of the water ice crystals within the clouds is overall constant over the year.

However, we observe in Figure 9b that some detections of particles with r_{eff} between 0.9 and 2.2 μm are associated with lower extinction values than the ones from the typical trend: $k_{\text{ext}} \sim 10^{-4}$–$10^{-3}$ km^{-1} instead of $k_{\text{ext}} \sim 10^{-2}$ km^{-1}. A noteworthy point is that most of these detections correspond to observations that have been mostly acquired either during the MY 34 GDS or during the regional dust storm in the Northern hemisphere in MY 35. In addition, even for lower size of ice crystals, the GDS detections are correlated with lower k_{ext} values. These observations with lower extinction values are associated with detections at higher altitudes than those typical for these sizes of crystals (cf. Figure 4b). Thus, while water ice clouds are observed at higher altitudes during dust storms, their ice crystal number density is lower than what is typically observed outside these events.

5 Comparison with the Mars PCM

Our dataset provides precise and systematic monitoring of the cloud altitude, effective radius, and extinction over two Martian years. Thus, these new observational constraints can be compared to predictions by numerical simulations such as GCMs. Here we will compare our results with the Mars PCM (Forget et al., 1999; Montmessin et al., 2002; Madeleine et al., 2012; Navarro et al., 2014). We will focus on the observations acquired during the second half of MY 35, a non-GDS year for which we have access to a climatology of the atmospheric dust distribution (Montabone et al., 2015, 2020).

Even though the size of the ice crystals within the clouds is among the quantities available from version 5 of the Mars PCM, the model sizes are systematically and significantly larger than the values retrieved in this study as well as in previous ones (e.g., Wolff & Clancy, 2003; Vincendon et al., 2011; Clancy et al., 2019; Stcherbinine et al., 2020; Luginin et al., 2020; Liuzzi et al., 2020). Investigations on this discrepancy are currently ongoing by the Mars PCM team. Thus, we do not discuss further the crystals' size here, but we instead focus on the altitude of the clouds, through the volume mixing ratio of H_2O ice crystals in the atmosphere.

5.1 Global comparison for MY 35

Figure 10 shows the comparison between the water ice clouds detected by ACS-MIR (left column) and predicted by the Mars PCM (right column) from $L_s = 140°$ to $L_s = 360°$ (MY 35) for three ranges of latitude (North and South high latitudes, mid-latitudes) in order to delineate the latitudinal from the seasonal trends.

We observe that the seasonal trend shown in the ACS-MIR data for the mid-southern latitudes (i.e., increase of the altitude of the clouds around the perihelion) in the panels c & e is well reproduced by the PCM (panels d & f). However, the strong increase observed in the altitude of the clouds associated with the regional dust storm in the Northern hemisphere is only reproduced for a few model profiles (panel b).

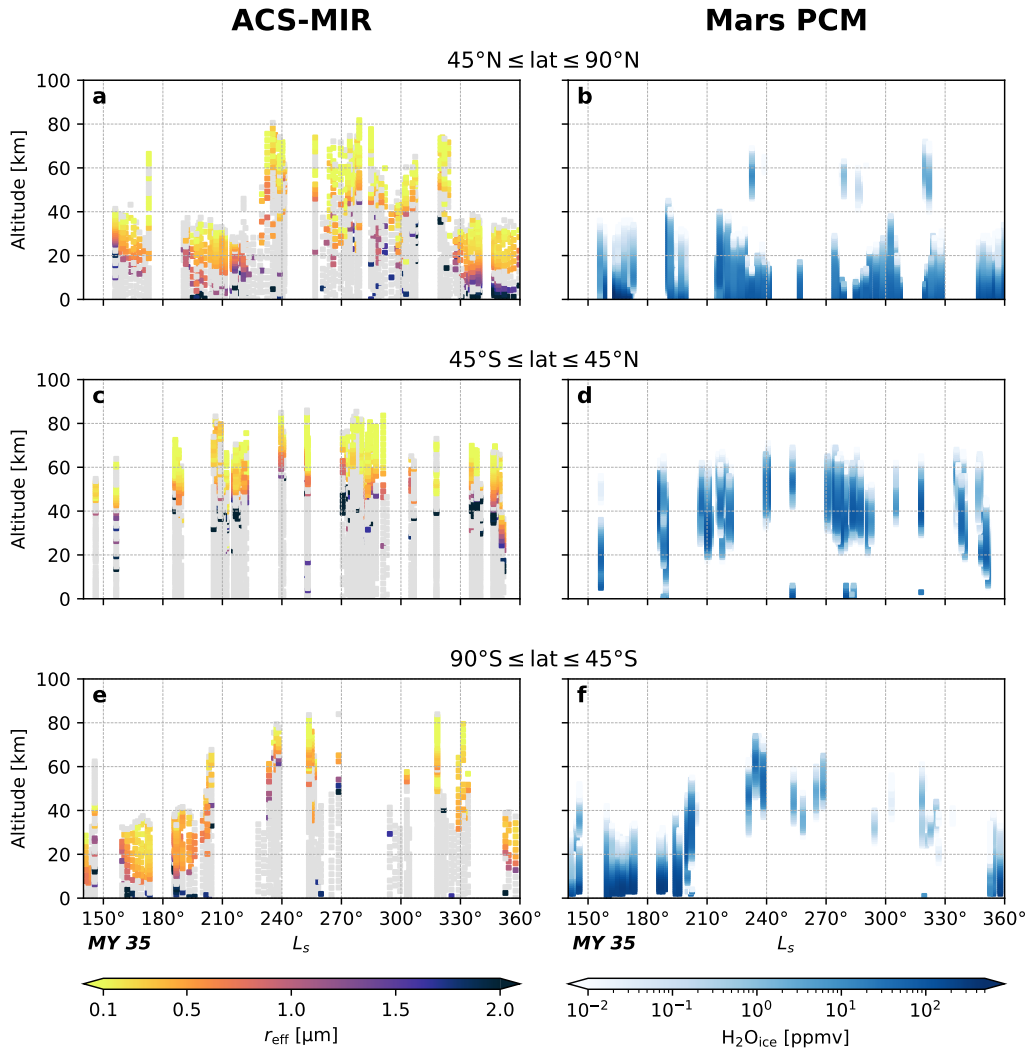

Figure 10. Comparison between the ACS-MIR cloud detections (left) and the water ice clouds predicted by the Mars PCM (right) over the second half of MY 35. Similarly to Figure 8 the profiles are filtered as a function of latitude in each panel to decorrelate between the seasonal and the latitudinal trends.

We also observe that in the polar regions, clouds are present in the PCM down to the surface while they are not detected at low altitudes in the ACS-MIR retrievals, which is not inconsistent. Indeed, as mentioned in Stcherbinine et al. (2020) our method is not sensitive to the larger ($r_{\text{eff}} \geq 2-3$ μm) ice particles, and to mixed dust-ice layers dominated by dust. Thus, it is likely that we do not detect some atmospheric layers with water ice crystals at the bottom of the profiles.

We observe another difference between the model and the data: the maximum altitude of the clouds in the PCM is usually lower than that observed: by ∼10 km in the polar regions and up to ∼20 km in the mid-latitudes. This difference is this time not linked with an observational bias (we detect more clouds layers than predicted by

the model). Further investigations are required to understand why the simulations do not reproduce precisely observed altitudes.

5.2 Comparison on individual profiles

Figure 11 presents a close-up view of the comparison between the ACS-MIR retrievals and the Mars PCM predictions for 6 individual profiles taken between $L_s = 121°$ and $L_s = 352°$ in MY 35. For each profile, the information about the altitude of the water ice cloud in both the ACS-MIR observation and the Mars PCM simulations are provided, as well as the extinction coefficient at $\lambda = 3.2$ µm.

We observe that the modeled extinction values (k_{ext}) at $\lambda = 3.2$ µm predicted by the model match the values retrieved by ACS-MIR, at least for the altitudes where the PCM produces clouds (panels a, c, d & e). However, we still note a shift of about 10 to 20 km in the altitudes where a cloud layer is typically detected versus where they are predicted by the PCM (panels a & f). Despite the limitations of our method, it is clear that ACS observes clouds higher than predicted by the PCM. Indeed, by looking at the ACS-MIR k_{ext} profiles, we suspect that some clouds layers are missing at the bottom of the clouds (panels a, e & f) as the detached layer that is visible in the extinction profile extends to a lower altitude than the water ice cloud detection. However, we note that when a cloud layer is not predicted to extend as high as it is observed by ACS, the model atmospheric extinction also decreases faster than the measured one (panels a & f), which strengthens the validity of the differences noted between PCM predictions and ACS observations for these altitudes. Plus, we also find that the largest discrepancies are observed for the higher altitude clouds, and seem likely to be to be related to the difficulty of the model to reproduce in general the high-altitude detached layers of water ice detected by ACS (panels b & d).

Thus, clouds predicted at lower altitudes in the Mars PCM compared to the ACS-MIR observations may be the manifestation of the limits of our retrieval method, while the lack of the upper layers in the PCM is a shortcoming in the current model.

6 Conclusion

In this paper, we present the results of our study on the identification and characterization of the Martian water ice clouds properties from IR SO data acquired by the ACS-MIR instrument onboard TGO between $L_s = 163°$ (MY 34) and $L_s = 181°$ (MY 36). Using the methodology previously described in Stcherbinine et al. (2020), we are able to simultaneously detect the presence of water ice clouds in the Martian atmosphere, and constrain the size of their crystals at each observed altitude. As TGO's orbit allows ACS to span all the latitudes between 80°S and 80°N in about $\sim 20°$ of L_s, this new dataset allows us to monitor the properties of the water ice clouds as a function of both the season and the latitude. In addition, the data acquired during MY 35 give us reference measurements at the same period to be compared to the observations acquired during the MY 34 GDS to better constrain the effects of such an event.

The main results are summarized below:

- The Solar Occultation technique used by ACS-MIR provides highly sensitive measurements that allow us to observe optically thin clouds ($k_{\text{ext}}(\lambda = 3.2\ \mu\text{m}) \sim 10^{-4}$ km^{-1}). Such clouds are typically much harder to detect through other observing geometries (on-disk or limb scattering).
- Where thick water ice clouds appear locally in the Martian atmosphere (Smith et al., 2013; Wolff et al., 2019; Szantai et al., 2021), our SO observations reveal the quasi-systematic presence of small water ice crystals within the upper layers

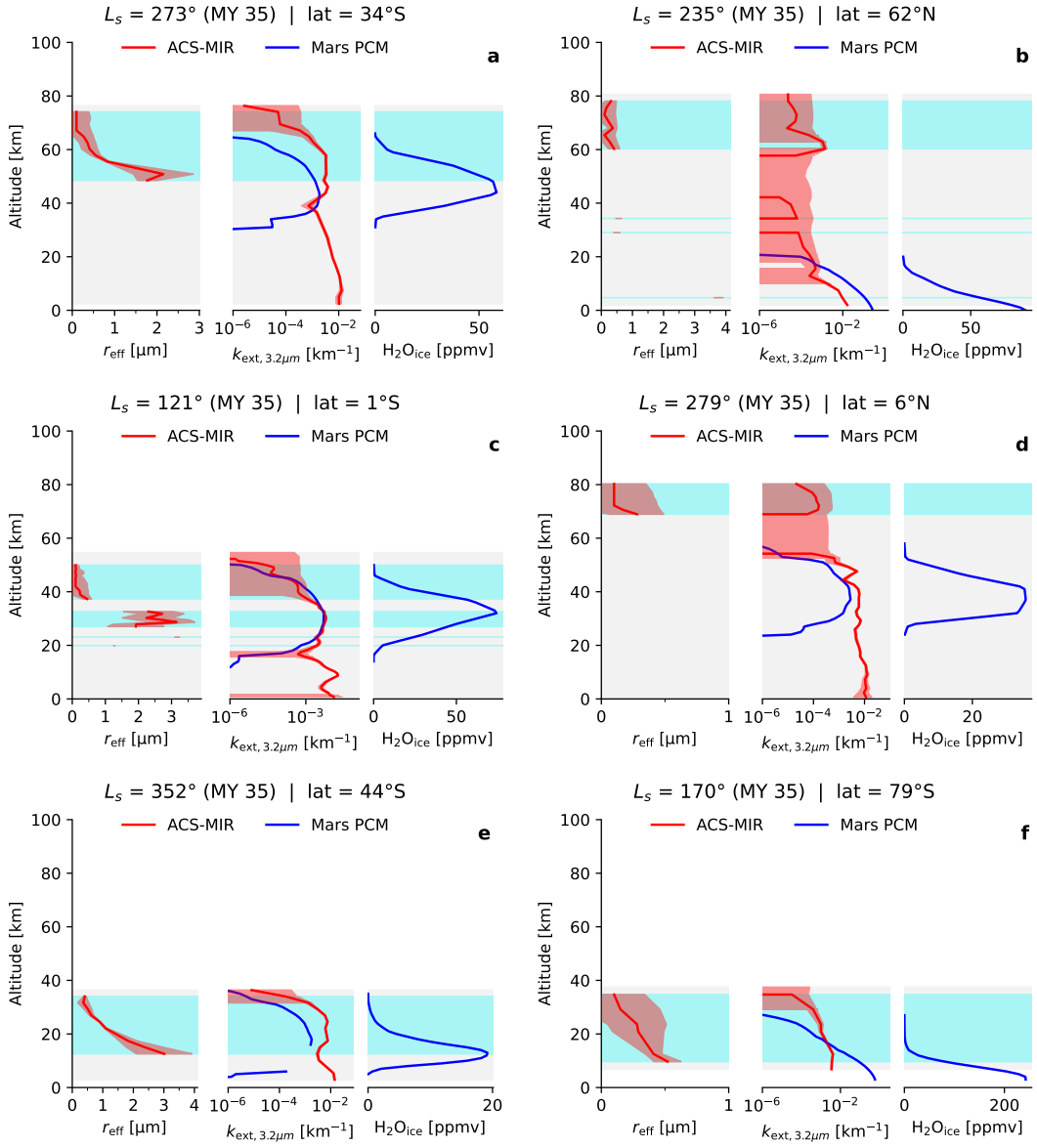

Figure 11. Comparison between the ACS-MIR retrieval (red lines) and the Mars PCM prediction (blue lines) for 6 individual profiles from MY 35. Each panel shows the water ice r_{eff} retrieved by ACS-MIR (left), the atmospheric extinction (k_{ext}) at λ = 3.2 µm (center) and the amount of water ice predicted by the Mars PCM (right). The light blue areas represent the altitudes where water ice clouds have been identified in the ACS-MIR data.

of the atmospheric aerosols (at least near the morning and evening terminators; i.e., at local times $\sim$ 06:00 and 18:00).

- The decrease of the ice crystals size as the altitude increases, previously noticed in the GDS study (Stcherbinine et al., 2020) and by other TGO studies (Luginin et al., 2020; Liuzzi et al., 2020), remains the observed behavior in this extended 2-MY dataset.
- The comparison between the perihelion periods of MY 34 and MY 35 allows us to contrast conditions during the MY 34 GDS with those of the same season in the absence of such a dramatic atmospheric event. It can be seen that the global altitude of the water ice clouds has increased by 10 km during the GDS compared to a more typical year, and this altitude increase can been 20 km for the smallest ice crystals ($r_{\text{eff}} \leq 0.1$ µm).
- No large-grained clouds ($r_{\text{eff}} \geq 1.5$ µm) have been observed at high altitudes (60 to 65 km range) during the non-GDS year, while they were detected during the MY 34 GDS. However, such clouds have been detected at 55 km (a relatively high altitude for such large ice crystals) close to the equator without being associated with a particular dust storm event.
- We also note that this elevation of the water ice clouds during a dust storm corresponds to a decrease of the typical extinction values associated with a specific ice crystal sizes.
- We observe variations of 20 to 40 km between the average altitude of the water ice clouds during summer and winter for both hemispheres, with water ice clouds often detected up to 80 km during summer seasons. The variations are stronger in the high latitudes compared to those in the equatorial regions.
- In addition to the seasonal variations, clouds are also detected typically 20 to 40 km higher close to the equator than in the polar regions.
- Finally, comparison between the ACS-MIR retrievals and the Mars PCM shows that the water ice clouds are usually predicted at lower altitudes in the model, up to 10 km lower in the polar regions and 20 km in the midlatitudes.

In conclusion, we investigated the impact of season and latitude on the altitude and the size of the water ice crystals. These results have been compared to predictions from climate models, showing a good agreement overall, while revealing some regions of discrepancies associated with the cloud altitudes. The quasi-systematic detection of water ice clouds in our observations highlights the importance of considering these clouds in studies of the current Martian atmosphere and climate.

Data Availability

Raw ACS data are available on the ESA PSA at `https://archives.esac.esa.int/psa/#!Table%20View/ACS=instrument`. Derived particles sizes and atmospheric extinction profiles can be found in Stcherbinine (2022).

Acknowledgments

ExoMars is a space mission of ESA and Roscosmos. The ACS experiment is led by IKI Space Research Institute in Moscow. The project acknowledges funding by Roscosmos and CNES. Science operations of ACS are funded by Roscosmos and ESA. Science support in IKI is funded by Federal agency of science organization (FANO). MJW acknowledges support from Jet Propulsion Laboratory subcontract contract 1551112.

References

Ball, E. R., Mitchell, D. M., Seviour, W. J. M., Thomson, S. I., & Vallis, G. K. (2021, September). The Roles of Latent Heating and Dust in the Structure

and Variability of the Northern Martian Polar Vortex. *The Planetary Science Journal*, *2*(5), 203. doi: 10.3847/PSJ/ac1ba2

Battalio, M., & Wang, H. (2021, January). The Mars Dust Activity Database (MDAD): A comprehensive statistical study of dust storm sequences. *Icarus*, *354*, 114059. doi: 10.1016/j.icarus.2020.114059

Clancy, R. T., Grossman, A. W., Wolff, M. J., James, P. B., Rudy, D. J., Billawala, Y. N., ... Muhleman, D. O. (1996, July). Water Vapor Saturation at Low Altitudes around Mars Aphelion: A Key to Mars Climate? *Icarus*, *122*(1), 36–62. doi: 10.1006/icar.1996.0108

Clancy, R. T., Montmessin, F., Benson, J., Daerden, F., Colaprete, A., & Wolff, M. J. (2017). Mars Clouds. In F. Forget, M. D. Smith, R. T. Clancy, R. W. Zurek, & R. M. Haberle (Eds.), *The Atmosphere and Climate of Mars* (pp. 76–105). Cambridge: Cambridge University Press. doi: 10.1017/9781139060172.005

Clancy, R. T., Wolff, M. J., Smith, M. D., Kleinböhl, A., Cantor, B. A., Murchie, S. L., ... Sandor, B. J. (2019, August). The distribution, composition, and particle properties of Mars mesospheric aerosols: An analysis of CRISM visible/near-IR limb spectra with context from near-coincident MCS and MARCI observations. *Icarus*, *328*, 246–273. doi: 10.1016/j.icarus.2019.03.025

D'Aversa, E., Oliva, F., Altieri, F., Sindoni, G., Carrozzo, F. G., Bellucci, G., ... Amoroso, M. (2022, January). Vertical distribution of dust in the martian atmosphere: OMEGA/MEx limb observations. *Icarus*, *371*, 114702. doi: 10.1016/j.icarus.2021.114702

Fedorova, A. A., Korablev, O. I., Bertaux, J. L., Rodin, A. V., Montmessin, F., Belyaev, D. A., & Reberac, A. (2009, March). Solar infrared occultation observations by SPICAM experiment on Mars-Express: Simultaneous measurements of the vertical distributions of H2O, CO2 and aerosol. *Icarus*, *200*(1), 96–117. doi: 10.1016/j.icarus.2008.11.006

Fedorova, A. A., Montmessin, F., Korablev, O., Luginin, M., Trokhimovskiy, A., Belyaev, D. A., ... Wilson, C. F. (2020, January). Stormy water on Mars: The distribution and saturation of atmospheric water during the dusty season. *Science*, eaay9522. doi: 10.1126/science.aay9522

Fedorova, A. A., Montmessin, F., Rodin, A. V., Korablev, O. I., Määttänen, A., Maltagliati, L., & Bertaux, J. L. (2014, March). Evidence for a bimodal size distribution for the suspended aerosol particles on Mars. *Icarus*, *231*, 239–260. doi: 10.1016/j.icarus.2013.12.015

Forget, F., Hourdin, F., Fournier, R., Hourdin, C., Talagrand, O., Collins, M., ... Huot, J.-P. (1999). Improved general circulation models of the Martian atmosphere from the surface to above 80 km. *Journal of Geophysical Research: Planets*, *104*(E10), 24155–24175. doi: 10.1029/1999JE001025

Forget, F., Millour, E., Bierjon, A., Delavois, A., Fan, S., Lange, L., ... the Mars PCM development teams (2022, June). Challenges in mars climate modelling with the LMD Mars Global Climate Model, now called the Mars "Planetary Climate Model" (PCM). In *Seventh international workshop on the Mars atmosphere: Modelling and observations* (pp. ??–??). Paris, France.

Forget, F., Millour, E., Spiga, A., Navarro, T., Madeleine, J. B., Pottier, A., ... Read, P. L. (2014, January). Simulating the Mars Climate with the LMD Mars Global Climate Model: Validation and issues. In *The Fifth International Workshop on the Mars Atmosphere: Modelling and Observation* (p. 1204). Oxford.

Gierasch, P. J., & Goody, R. M. (1972, March). The Effect of Dust on the Temperature of the Martian Atmosphere. *Journal of the Atmospheric Sciences*, *29*(2), 400–402. doi: 10.1175/1520-0469(1972)029<0400:TEODOT>2.0.CO;2

Goldman, A., & Saunders, R. (1979, February). Analysis of atmospheric infrared spectra for altitude distribution of atmospheric trace constituents—I. Method

of analysis. *Journal of Quantitative Spectroscopy and Radiative Transfer*, *21*(2), 155–161. doi: 10.1016/0022-4073(79)90027-X

Guzewich, S. D., Smith, M. D., & Wolff, M. J. (2014, December). The vertical distribution of Martian aerosol particle size: Vertical Profile of Mars Aerosol Size. *Journal of Geophysical Research: Planets*, *119*(12), 2694–2708. doi: 10.1002/2014JE004704

Haberle, R. M., Montmessin, F., Kahre, M. A., Hollingsworth, J. L., Schaeffer, J., Wolff, M. J., & Wilson, R. J. (2011, February). Radiative Effects of Water Ice Clouds on the Martian Seasonal Water Cycle. In *Fourth international workshop on the Mars atmosphere: Modelling and observations* (pp. 223–226). Paris, France.

Hansen, J. E., & Travis, L. D. (1974, October). Light scattering in planetary atmospheres. *Space Science Reviews*, *16*(4), 527–610. doi: 10.1007/BF00168069

Heavens, N. G., Richardson, M. I., Kleinböhl, A., Kass, D. M., McCleese, D. J., Abdou, W., ... Wolkenberg, P. M. (2011). The vertical distribution of dust in the Martian atmosphere during northern spring and summer: Observations by the Mars Climate Sounder and analysis of zonal average vertical dust profiles. *Journal of Geophysical Research: Planets*, *116*(E4). doi: 10.1029/2010JE003691

Jaquin, F., Gierasch, P., & Kahn, R. (1986, December). The vertical structure of limb hazes in the Martian atmosphere. *Icarus*, *68*(3), 442–461. doi: 10.1016/0019-1035(86)90050-3

Kleinböhl, A., Schofield, J. T., Kass, D. M., Abdou, W. A., & McCleese, D. J. (2015, November). No widespread dust in the middle atmosphere of Mars from Mars Climate Sounder observations. *Icarus*, *261*, 118–121. doi: 10.1016/j.icarus.2015.08.010

Korablev, O., Montmessin, F., Trokhimovskiy, A., Fedorova, A. A., Shakun, A. V., Grigoriev, A. V., ... Zorzano, M. P. (2018, February). The Atmospheric Chemistry Suite (ACS) of Three Spectrometers for the ExoMars 2016 Trace Gas Orbiter. *Space Science Reviews*, *214*(1), 7. doi: 10.1007/s11214-017-0437-6

Korablev, O., Vandaele, A. C., Montmessin, F., Fedorova, A. A., Trokhimovskiy, A., Forget, F., ... The ACS and NOMAD Science Team (2019, April). No detection of methane on Mars from early ExoMars Trace Gas Orbiter observations. *Nature*, *568*(7753), 517–520. doi: 10.1038/s41586-019-1096-4

Lemmon, M. T., Wolff, M. J., Bell, J. F., Smith, M. D., Cantor, B. A., & Smith, P. H. (2015, May). Dust aerosol, clouds, and the atmospheric optical depth record over 5 Mars years of the Mars Exploration Rover mission. *Icarus*, *251*, 96–111. doi: 10.1016/j.icarus.2014.03.029

Liuzzi, G., Villanueva, G. L., Crismani, M. M. J., Smith, M. D., Mumma, M. J., Daerden, F., ... Patel, M. R. (2020). Strong Variability of Martian Water Ice Clouds During Dust Storms Revealed From ExoMars Trace Gas Orbiter/NOMAD. *Journal of Geophysical Research: Planets*, *125*(4), e2019JE006250. doi: 10.1029/2019JE006250

Liuzzi, G., Villanueva, G. L., Trompet, L., Crismani, M. M. J., Piccialli, A., Aoki, S., ... Vandaele, A. C. (2021). First Detection and Thermal Characterization of Terminator CO2 Ice Clouds With ExoMars/NOMAD. *Geophysical Research Letters*, *48*(22), e2021GL095895. doi: 10.1029/2021GL095895

Luginin, M., Fedorova, A., Ignatiev, N., Trokhimovskiy, A., Shakun, A., Grigoriev, A., ... Korablev, O. (2020). Properties of Water Ice and Dust Particles in the Atmosphere of Mars During the 2018 Global Dust Storm as Inferred From the Atmospheric Chemistry Suite. *Journal of Geophysical Research: Planets*, *125*(11), e2020JE006419. doi: 10.1029/2020JE006419

Määttänen, A., Listowski, C., Montmessin, F., Maltagliati, L., Reberac, A., Joly, L., & Bertaux, J.-L. (2013, April). A complete climatology of the aerosol verti-

cal distribution on Mars from MEx/SPICAM UV solar occultations. *Icarus*, *223*(2), 892–941. doi: 10.1016/j.icarus.2012.12.001

Madeleine, J.-B., Forget, F., Millour, E., Montabone, L., & Wolff, M. J. (2011). Revisiting the radiative impact of dust on Mars using the LMD Global Climate Model. *Journal of Geophysical Research: Planets*, *116*(E11). doi: 10.1029/2011JE003855

Madeleine, J.-B., Forget, F., Millour, E., Navarro, T., & Spiga, A. (2012). The influence of radiatively active water ice clouds on the Martian climate. *Geophysical Research Letters*, *39*(23). doi: 10.1029/2012GL053564

Maltagliati, L., Montmessin, F., Fedorova, A., Korablev, O., Forget, F., & Bertaux, J.-L. (2011, September). Evidence of Water Vapor in Excess of Saturation in the Atmosphere of Mars. *Science*, *333*(6051), 1868–1871. doi: 10.1126/science.1207957

Michelangeli, D. V., Toon, O. B., Haberle, R. M., & Pollack, J. B. (1993, April). Numerical Simulations of the Formation and Evolution of Water Ice Clouds in the Martian Atmosphere. *Icarus*, *102*(2), 261–285. doi: 10.1006/icar.1993.1048

Montabone, L., Forget, F., Millour, E., Wilson, R., Lewis, S., Cantor, B., ... Wolff, M. (2015, May). Eight-year climatology of dust optical depth on Mars. *Icarus*, *251*, 65–95. doi: 10.1016/j.icarus.2014.12.034

Montabone, L., Spiga, A., Kass, D. M., Kleinböhl, A., Forget, F., & Millour, E. (2020). Martian Year 34 Column Dust Climatology from Mars Climate Sounder Observations: Reconstructed Maps and Model Simulations. *Journal of Geophysical Research: Planets*, *125*(8), e2019JE006111. doi: 10.1029/2019JE006111

Montmessin, F., Forget, F., Rannou, P., Cabane, M., & Haberle, R. M. (2004). Origin and role of water ice clouds in the Martian water cycle as inferred from a general circulation model. *Journal of Geophysical Research: Planets*, *109*(E10). doi: 10.1029/2004JE002284

Montmessin, F., Quémerais, E., Bertaux, J. L., Korablev, O., Rannou, P., & Lebonnois, S. (2006). Stellar occultations at UV wavelengths by the SPICAM instrument: Retrieval and analysis of Martian haze profiles. *Journal of Geophysical Research*, *111*(E9). doi: 10.1029/2005JE002662

Montmessin, F., Rannou, P., & Cabane, M. (2002). New insights into Martian dust distribution and water-ice cloud microphysics. *Journal of Geophysical Research: Planets*, *107*(E6), 4-1-4-14. doi: 10.1029/2001JE001520

Montmessin, F., Smith, M. D., Langevin, Y., Mellon, M. T., & Fedorova, A. (2017). The Water Cycle. In F. Forget, M. D. Smith, R. T. Clancy, R. W. Zurek, & R. M. Haberle (Eds.), *The Atmosphere and Climate of Mars* (pp. 338–373). Cambridge: Cambridge University Press. doi: 10.1017/9781139060172.011

Navarro, T., Madeleine, J.-B., Forget, F., Spiga, A., Millour, E., Montmessin, F., & Määttänen, A. (2014). Global climate modeling of the Martian water cycle with improved microphysics and radiatively active water ice clouds. *Journal of Geophysical Research: Planets*, *119*(7), 1479–1495. doi: 10.1002/2013JE004550

Olsen, K. S., Lefèvre, F., Montmessin, F., Fedorova, A. A., Trokhimovskiy, A., Baggio, L., ... Shakun, A. (2021, February). The vertical structure of CO in the Martian atmosphere from the ExoMars Trace Gas Orbiter. *Nature Geoscience*, *14*(2), 67–71. doi: 10.1038/s41561-020-00678-w

Poncin, L., Kleinböhl, A., Kass, D. M., Clancy, R. T., Aoki, S., & Vandaele, A. C. (2022, March). Water vapor saturation and ice cloud occurrence in the atmosphere of Mars. *Planetary and Space Science*, *212*, 105390. doi: 10.1016/j.pss.2021.105390

Richardson, M. I. (2002). Water ice clouds in the Martian atmosphere: General circulation model experiments with a simple cloud scheme. *Journal of Geophysical Research*, *107*(E9). doi: 10.1029/2001JE001804

Rossi, L., Vals, M., Alday, J., Montmessin, F., Fedorova, A., Trokhimovskiy, A., ... Millour, E. (2022). The HDO Cycle on Mars: Comparison of ACS Observations With GCM Simulations. *Journal of Geophysical Research: Planets*, *127*(8), e2022JE007201. doi: 10.1029/2022JE007201

Smith, M. D., Wolff, M. J., Clancy, R. T., Kleinböhl, A., & Murchie, S. L. (2013, February). Vertical distribution of dust and water ice aerosols from CRISM limb-geometry observations: CRISM LIMB AEROSOLS. *Journal of Geophysical Research: Planets*, *118*(2), 321–334. doi: 10.1002/jgre.20047

Stcherbinine, A. (2022). *A Two Martian Years Survey of Water Ice Clouds on Mars with ACS onboard TGO* [dataset]. Mendeley Data. (v1) doi: 10.17632/hff8kc6fsy.1

Stcherbinine, A., Vincendon, M., Montmessin, F., Wolff, M. J., Korablev, O., Fedorova, A., ... Shakun, A. (2020). Martian Water Ice Clouds During the 2018 Global Dust Storm as Observed by the ACS-MIR Channel Onboard the Trace Gas Orbiter. *Journal of Geophysical Research: Planets*, *125*(3), e2019JE006300. doi: 10.1029/2019JE006300

Streeter, P. M., Sellers, G., Wolff, M. J., Mason, J. P., Patel, M. R., Lewis, S. R., ... López-Moreno, J. J. (2022). Vertical Aerosol Distribution and Mesospheric Clouds From ExoMars UVIS. *Journal of Geophysical Research: Planets*, *127*(5), e2021JE007065. doi: 10.1029/2021JE007065

Szantai, A., Audouard, J., Forget, F., Olsen, K. S., Gondet, B., Millour, E., ... Bibring, J.-P. (2021, January). Martian cloud climatology and life cycle extracted from Mars Express OMEGA spectral images. *Icarus*, *353*, 114101. doi: 10.1016/j.icarus.2020.114101

Toigo, A. D., Waugh, D. W., & Guzewich, S. D. (2020, September). Atmospheric transport into polar regions on Mars in different orbital epochs. *Icarus*, *347*, 113816. doi: 10.1016/j.icarus.2020.113816

Toon, O. B., & Ackerman, T. P. (1981, October). Algorithms for the calculation of scattering by stratified spheres. *Applied Optics*, *20*(20), 3657. doi: 10.1364/AO.20.003657

Trokhimovskiy, A., Korablev, O., Ivanov, Y. S., Siniyavsky, I. I., Fedorova, A., Stepanov, A. V., ... Montmessin, F. (2015, September). Middle-infrared echelle cross-dispersion spectrometer ACS-MIR for the ExoMars Trace Gas Orbiter. In M. Strojnik Scholl & G. Páez (Eds.), *SPIE Optical Engineering + Applications* (p. 960808). San Diego, California, United States. doi: 10.1117/12.2190359

Trokhimovskiy, A., Perevalov, V., Korablev, O., Fedorova, A. A., Olsen, K. S., Bertaux, J.-L., ... Lukashevskaya, A. (2020, July). First observation of the magnetic dipole CO2 absorption band at 3.3 Mm in the atmosphere of Mars by the ExoMars Trace Gas Orbiter ACS instrument. *Astronomy & Astrophysics*, *639*, A142. doi: 10.1051/0004-6361/202038134

Vals, M., Forget, F., Spiga, A., & Millour, E. (2018, September). Impact of the refinement of the vertical resolution on the simulation of the water cycle by the martian LMD Global Climate Model. *European Planetary Science Congress*, *12*, EPSC2018-847.

Vals, M., Rossi, L., Montmessin, F., Lefèvre, F., Gonzalez-Galindo, F., Fedorova, A., ... Montabone, L. (2022). Improved Modeling of Mars' HDO Cycle Using a Mars' Global Climate Model. *Journal of Geophysical Research: Planets*, *127*(8), e2022JE007192. doi: 10.1029/2022JE007192

Vandaele, A. C., Korablev, O., Daerden, F., Aoki, S., Thomas, I. R., Altieri, F., ... ACS Science Team (2019, April). Martian dust storm impact on atmospheric H2O and D/H observed by ExoMars Trace Gas Orbiter. *Nature*, *568*(7753), 521–525. doi: 10.1038/s41586-019-1097-3

Vincendon, M., Pilorget, C., Gondet, B., Murchie, S., & Bibring, J.-P. (2011, November). New near-IR observations of mesospheric CO $_2$ and H $_2$ O clouds

on Mars. *Journal of Geophysical Research*, *116*. doi: 10.1029/2011JE003827

Wang, C., Forget, F., Bertrand, T., Spiga, A., Millour, E., & Navarro, T. (2018). Parameterization of Rocket Dust Storms on Mars in the LMD Martian GCM: Modeling Details and Validation. *Journal of Geophysical Research: Planets*, *123*(4), 982–1000. doi: 10.1002/2017JE005255

Wang, H., & Richardson, M. I. (2015, May). The origin, evolution, and trajectory of large dust storms on Mars during Mars years 24–30 (1999–2011). *Icarus*, *251*, 112–127. doi: 10.1016/j.icarus.2013.10.033

Wilson, R. J., Lewis, S. R., Montabone, L., & Smith, M. D. (2008). Influence of water ice clouds on Martian tropical atmospheric temperatures. *Geophysical Research Letters*, *35*(7). doi: 10.1029/2007GL032405

Wilson, R. J., Neumann, G. A., & Smith, M. D. (2007). Diurnal variation and radiative influence of Martian water ice clouds. *Geophysical Research Letters*, *34*(2). doi: 10.1029/2006GL027976

Wolff, M. J., & Clancy, R. T. (2003). Constraints on the size of Martian aerosols from Thermal Emission Spectrometer observations. *Journal of Geophysical Research: Planets*, *108*(E9). doi: 10.1029/2003JE002057

Wolff, M. J., Clancy, R. T., Kahre, M. A., Haberle, R. M., Forget, F., Cantor, B. A., & Malin, M. C. (2019, November). Mapping water ice clouds on Mars with MRO/MARCI. *Icarus*, *332*, 24–49. doi: 10.1016/j.icarus.2019.05.041

Wolff, M. J., Lopéz-Valverde, M., Madeleine, J.-B., Wilson, R. J., Smith, M. D., Fouchet, T., & Delory, G. T. (2017). Radiative Process: Techniques and Applications. In F. Forget, M. D. Smith, R. T. Clancy, R. W. Zurek, & R. M. Haberle (Eds.), *The Atmosphere and Climate of Mars* (pp. 106–171). Cambridge: Cambridge University Press. doi: 10.1017/9781139060172.006